THE ASTROPHYSICAL JOURNAL, 900:194 (7pp), 2020 September 10 https://doi.org/10.3847/1538-4357/aba902

Study of Eclipses for Redback Pulsar J1227–4853

Sanjay Kudale[1], Jayanta Roy[1], Bhaswati Bhattacharyya[1], Ben Stappers[2], and Jayaram Chengalur[1]
[1] National Centre for Radio Astrophysics, Tata Institute of Fundamental Research, Pune 411 007, India
[2] Jodrell Bank Centre for Astrophysics, School of Physics and Astronomy, The University of Manchester, Manchester M13 9PL, UK
Received 2020 March 20; revised 2020 July 13; accepted 2020 July 17; published 2020 September 15

Abstract

We present a multifrequency study of eclipse properties of a transitional redback millisecond pulsar J1227−4853 discovered in 2014 with the GMRT. Emission from this pulsar is eclipsed at 607 MHz for about 37% of its orbit around the superior conjunction. We observe eclipse ingress and egress transitions that last for 12% and 15% of its orbit, respectively, resulting in only 36% of the orbit being unaffected by eclipsing material. We report an excess dispersion measure (DM) at eclipse boundaries of 0.079(3) pc cm^{-3}, and the corresponding electron column density (N_e) is 24.4(8) $\times$ 10^{16} cm^{-2}. Simultaneous timing and imaging studies suggest that the eclipses in J1227−4853 are not caused by temporal smearing due to excess dispersion and scattering but could be caused by removal of pulsar flux due to cyclotron absorption of the pulsed signal by intra-binary material constraining the companion's magnetic field. Additionally, near the inferior conjunction at orbital phases 0.71 and 0.82 the pulsed emission is significantly delayed, which is associated with a fading of the pulsed and continuum flux densities. At orbital phase ∼0.82, we measure a change in DM of 0.035(3) pc cm^{-3} and N_e of 10.8(8) $\times$ 10^{16} cm^{-2} associated with a dimming of up to ∼30% of the peak flux density. Such flux fading around a fixed orbital phase is not reported for other eclipsing binaries. Moreover, this event around the inferior conjunction could be caused by absorption of the pulsed signal by fragmented blobs of plasma generated from mass loss through the L2 Lagrangian point.

Unified Astronomy Thesaurus concepts: Accretion (14); Binary pulsars (153); Eclipses (442); Millisecond pulsars (1062)

1. Introduction

Millisecond pulsars (MSPs) are believed to be generated in a recycling process where the pulsar accretes mass from its companion star in a close binary system resulting in a faster spin period via transfer of angular momentum (e.g., Bhattacharya 1992). A special class of fast spinning MSPs (spin period <8 ms) in evolving compact binaries (less than a day), where the pulsar is in active interaction with its companion are classified as black widow and redback MSP systems. Such compact systems where companions are ablated away by energetic pulsar winds, are in general referred to as spider MSPs. In the majority of such systems, the inclinations of the binaries allow the intra-binary material to obscure the pulsar emission for part of its orbit resulting in the observed eclipses. The volume occupied by the eclipsing material is well outside the companion's Roche lobe, and thus is not gravitationally bound to the companion. The energy of an isotropic pulsar wind at the distance of the companion is given by $\dot{E}/a^2$, where $\dot{E}$ is the spin-down energy of the pulsar and a is the distance to the companion. $\dot{E}/a^2$ in redback and black widow pulsars are $\sim 10^{34}$ erg/s/$R_\odot^2$, whereas $\dot{E}/a^2$ for canonical MSPs is around 10^{29}–10^{30} erg/s/$R_\odot^2$. Roy et al. (2015) reported the discovery of a 1.69 MSP J1227−4853, at a dispersion measure (DM) of 43.4 pc cm^{-3} associated with LMXB XSS J12270−4859, using the GMRT at 607 MHz. PSR J1227−4853 is in a 6.9 hr orbit with a companion of mass 0.17–0.46 $M_\odot$ and is eclipsed for a large fraction of its orbit at 607 MHz.

The majority of black widow and redback pulsars exhibit long eclipses (>10% of the orbital period) near their companion's superior conjunctions. Thompson et al. (1994) gives a detailed prescription for investigation of the eclipse mechanism in such systems. However, the detailed study of the eclipse properties have been performed for only a few of the spider pulsars: PSR J1544+4937 (Bhattacharyya et al. 2013), PSR B1744-24A (Lyne et al. 1990; Nice & Thorsett 1992; Bilous et al. 2019), PSR J1810+1744 (Polzin et al. 2018), PSR J1816+4510 (Polzin et al. 2020), B1957+20 (Fruchter et al. 1988; Ryba & Taylor 1991; Main et al. 2018; Li et al. 2019), and J2051−0827 (Stappers et al. 1996; Polzin et al. 2020). This could be due to the lack of available sensitive instruments operating at low frequencies, where the effects of eclipses are expected to be larger. This is addressed by some of the more recent studies (e.g., Main et al. 2018; Polzin et al. 2018, 2020; Li et al. 2019) with sensitive observations using the Arecibo, LOFAR, upgraded GMRT (uGMRT), and the Parkes telescope.

In this paper we present a detailed study of the eclipses in the PSR J1227−4853 system at multiple frequencies. Section 2 details the observations and analysis procedure. The subsections of Section 3 present the results from studies of the eclipse properties of PSR J1227−4853. Section 3.1 concentrates on the main eclipses at 607 MHz. Investigation of frequency dependent eclipsing is presented in Section 3.2. In addition to the main eclipse, we also observe excess dispersion around the inferior conjunction, which is reported in Section 3.3. Flux fading observed at eclipse ingress and around the inferior conjunction is reported in Section 3.4. A discussion of these results and a summary are presented in Section 4.

2. Observation and Analysis

Following the discovery, PSR J1227−4853 has been regularly observed using the GMRT coherent array at 607 MHz. Most of the observations reported in this paper were carried out with the legacy GMRT system using GMRT Software Back-end (GSB; Roy et al. 2010). We generated filter-bank data products having 512 × 0.0651 MHz channels at a 61.44 μs time resolution. These data were incoherently dedispersed at the pulsar DM and folded with the ephemeris using PRESTO (Ransom et al. 2002). We used a multi-Gaussian template for extracting times of arrival (TOAs) at each observing epoch. The TOAs were typically generated with an ∼4 minute integration time to achieve optimal signal-to-noise (S/N) as well as a time resolution sufficient to probe the eclipse transition. A similar time resolution was used in the imaging analysis (described below). PSR J1227−4853 is eclipsed for around 2.8 hr, which is ∼40% of its orbit (Roy et al. 2015). Many of the timing observations, typically of ∼1 hr duration and regularly performed with the GMRT, partially sample the eclipse phase allowing us to probe eclipse characteristics of PSR J1227−4853.

In order to probe the frequency dependence of eclipse characteristics we observed PSR J1227−4853 simultaneously at 300–500 and 550–750 MHz using the upgraded GMRT (uGMRT; Gupta et al. 2017). The increase of instantaneous bandwidth compensates for the reduction of the coherent array gain compared to our earlier observations resulting from splitting antennas into two subarrays. The 550–750 MHz data were recorded in 4096 × 0.0488 MHz filter-bank output at 81.92 μs time resolution, which was incoherently dedispersed and folded. Whereas 300–500 MHz data was recorded in 512 × 0.390 MHz coherently dedispersed filter-bank format at 10.24 μs time resolution in order to avoid residual dispersion smearing reducing the TOA uncertainties.

Visibility data were recorded with ∼2 s time resolution in parallel with the beam-formed data. Every observation of the target pulsar is accompanied with an observation of the phase calibrator 1154–350, which is sufficiently close and strong enough to perform bandpass and gain calibration (7.8 Jy). A continuum imaging analysis is carried out using an automated imaging pipeline (S. Kudale et al. 2020, in preparation) which is composed of *flagcal* (Chengalur 2013), *PyBDSM* (Mohan & Rafferty 2015), and *CASA*.[3] In total three self-calibration and imaging cycles are carried out, of which the first two cycles of gain calibration were done with phase-only calibration and the last was done with amplitude and phase calibration. Final imaging after the last self-calibration cycle is done only for the duration for which the pulsar was in the non-eclipsing phase of its orbit. This enabled us to estimate the average flux density on the given observation epoch. The self-calibrated uvdata were then used to generate snapshot images of the pulsar with an average time duration ∼3 minutes to generate the lightcurve. Since the pulsar is a point source, we use the peak flux density obtained by fitting a 2D Gaussian to the pulsar image to estimate pulsar flux density. This was done using the *imfit* task of CASA, with the same region box around the pulsar used to do the fit in all image frames. To obtain errorbars on the flux densities we used the task *imstat* of *CASA* to estimate the rms near the pulsar location. We feel that this is a conservative but better estimate of the true uncertainty than the formal error to the peak of the Gaussian fit.

3. Results

Even though the orbital period of PSR J1227−4853 is ∼6.9 hr, the source is visible at the GMRT sky for only ∼3.5 hr. Each observing session, typically of 1 hr duration, covers only a part of the orbital phase. However, regular timing observations performed with the GMRT allowed us to use this collection of observations to probe eclipse boundaries. Similar to Figure 1 by Polzin et al. (2019), we show a schematic diagram of the companion's orbit for the PSR J1227−4853 system highlighting the companion's Roche lobe ($R_L = 0.51$ $R_\odot$, Eggleton 1983, using 1.4 $M_\odot$ as pulsar mass and 0.2 $M_\odot$ as companion mass) eclipse regions at 591–624 MHz and 300–500 MHz. The observed flux fading near the inferior conjunction associated with increase of the line-of-sight DM is also indicated in this figure. We describe the main results from multifrequency investigation of PSR J1227−4853 in the following sections.

3.1. Study of Eclipses at 591–624 MHz

Our sample consists of 13 epochs of observations at 591–624 MHz, out of which six observations include an eclipse ingress and seven observations include an eclipse egress. Timing residuals of these observations are presented in Figure 2. We observed substantial delays in the timing residuals (888(28) μs) due to line-of-sight excess DMs at the eclipse boundaries associated with corresponding drops in the flux density. Moreover, we find that the eclipse ingress and egress transitions are spread over a range of orbital phases as shown by the shaded regions in Figure 2. The eclipse ingress transition starts from $\phi_B = 0.95$ and ends at 0.07, resulting in total ingress duration of 0.12 in the orbital phase. Using the detection at the latest ingress phase (ϕ_B∼ 0.07) and the earliest egress phase (ϕ_B∼ 0.44) from a sample of 13 eclipses, we estimate the duration of the completely eclipsed phase to be 37% of the orbital period. This duration is smaller than the value reported in Roy et al. (2015), which was based on a single ingress and egress detection. The egress transition region is spread over an orbital range from 0.44 to 0.59, resulting in a total egress side transition duration of 0.15 in the orbital phase. Thus the egress transition is seen for a longer duration compared to the ingress transition (by 12.4 ± 3 minutes), which is also seen in other eclipsing binary systems, e.g., PSR J1810+1744 (Polzin et al. 2018) and PSR J1544+4937 (Bhattacharyya et al. 2013). We find the center of the nondetection eclipse (excluding eclipse transitions) at an orbital phase of 0.255(5), which matches with the superior conjunction orbital phase. The estimated line-of-sight excess DM and the electron column density (N_e) from timing residuals are shown in Figure 2. The full eclipse and eclipse transition zones (shaded regions) seen in Figure 2 can also be visualized in the schematic top view of the eclipse geometry in Figure 1, where these regions are highlighted in dark purple and purple colors respectively.

The maximum delay in timing residuals around eclipse transitions detected for PSR J1227−4853 is 888(28) μs at 591–624 MHz. This gives excess DM of 0.079(3) pc cm^{-3} and N_e of 24.4(8) × 10^{16} cm^{-2} (see Figure 2). We estimate the corresponding electron density in the eclipse region (n_e∼ N_e/a) as 1.5 × 10^6 cm^{-3}, which is at least an order of magnitude higher than the electron density expected in the stellar wind (according to Johnstone et al. 2015, n_e due to the stellar wind at a distance similar to a is ∼10^5 cm^{-3}). This indicates that ablation from the companion is significantly contributing to the intra-binary material causing eclipses. This system also exhibits eclipses for a longer fraction of the orbital phase. We compare the eclipse properties of PSR J1227−4853 with the known eclipsing binaries in Section 4.

[3] https://casa.nrao.edu/

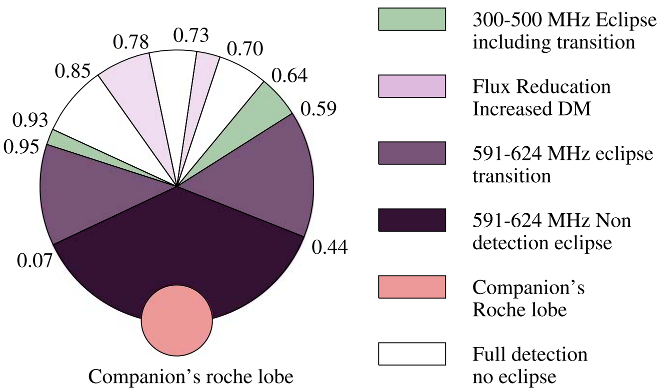

Figure 1. Top view of the companion's Roche lobe and geometry of the eclipsing binary. The companion's Roche lobe and orbit are approximately to scale, assuming the radio timing model (Roy et al. 2015).

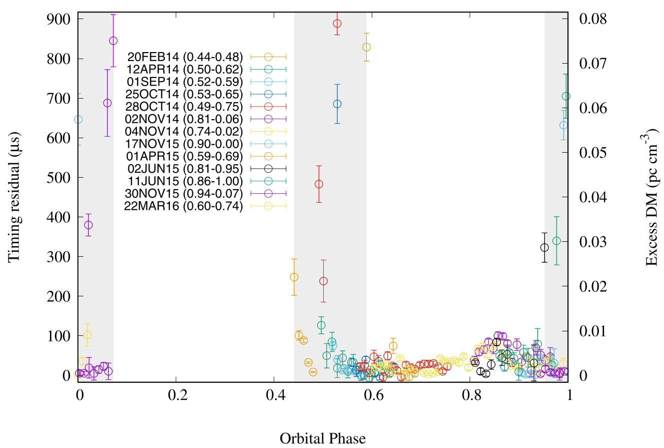

Figure 2. Variation of timing residual and DM with orbital phase on 13 observing epochs (denoted by different colors) at 591–624 MHz, individual epochs covering a small range of full orbital phase, but collectively the full orbital phase range is covered with all the observations.

3.2. Simultaneous Dual Frequency Study of Eclipses

In order to probe the frequency dependence of the eclipse duration for PSR J1227−4853 we carried out simultaneous dual-frequency observations at 300–500 and 550–750 MHz using the uGMRT. Observations performed on 2019 May 14 and 24 allowed us to probe the eclipse ingress and egress transitions respectively. This eliminates the effect of temporal variations of eclipse boundaries (as seen in Figure 2) while estimating the frequency dependence of the eclipse duration. The eclipse region for 300–500 MHz is shown by the light green color in Figure 1. Variation of the excess DM and N_e with orbital phase derived from the best-fit timing residuals are shown in Figure 3. Eclipse boundaries are marked by vertical lines: red for 300–500 MHz and blue for 550–750 MHz. We observe a larger eclipse duration at the lower frequency band (i.e.,∼1.2 times longer for 300–500 MHz band than 550–750 MHz band) and we note a possible asymmetry in frequency dependence of eclipse transitions in ingress and egress phase in the 300–500 MHz band compared to that in the 550–750 MHz band. The ingress starts earlier,$\delta t_{\rm ingress} = 11.86 \pm 0.5$ minutes, and egress ends later, $\delta t_{\rm egress} = 44.57 \pm 0.5$ minutes, at 300–500 MHz. If we consider a power-law dependence of eclipse duration with frequency ($T_{\rm eclipse}\ \alpha\ \nu^n$), we estimate a power-law index of $n = -0.44$ from these simultaneous observations. Frequency dependent eclipse durations are observed for some of the other eclipsing binaries as well. Earlier studies report that at lower frequencies the eclipse duration is seen to be larger compared to that of higher frequencies for a given system. We have listed excess DM, pulsar wind flux ($\dot{E}/a^2$), eclipse duration, and power-law index for eclipsing binaries in Table 1. We observed an asymmetry in eclipse boundaries between the two observing bands where $\delta t_{\rm egress} > \delta t_{\rm ingress}$ by 32.7 ± 0.7 minutes. From this we can derive separate power-law frequency dependence for ingress ($T_{\rm ingress}\ \alpha\ \nu^{n_i}$) and egress ($T_{\rm egress}\ \alpha\ \nu^{n_e}$) transitions (w.r.t superior conjunction), where $n_i = -0.19$ and $n_e = -0.66$.

3.3. Excess Dispersion around Inferior Conjunction

In addition to eclipses seen at orbital phases from 0.95 up to 0.59, PSR J1227−4853 exhibits occasional occurrences of residual delays around ϕ_B of ∼0.7 and ∼0.8 (marked by the light purple color in the eclipse geometry in Figure 1). This is well outside the eclipse regions, centered around inferior conjunction, $\phi_B = 0.75$ (seen in the top panel of Figure 4). The largest excess DM and N_e we measured at $\phi_B = 0.82$ is 0.0199(6) pc cm^{-3} and $6.1(2) \times 10^{16}$ cm^{-2} respectively, which is a factor of 4 lower than the values measured at the eclipse boundaries. Whereas at $\phi_B = 0.71$ we measured an excess DM of 0.0037(6) pc cm^{-3} and N_e of $1.1(2) \times 10^{16}$ cm^{-2}. The durations of these phenomenon of excess dispersion measured at ϕ_B of 0.7 and 0.8 are 11.5 ± 1.7 and 27.1 ± 1.7 minutes respectively. We present three epochs of coherently dedispersed observations at 550–750 MHz probing excess dispersion around ϕ_B of 0.82 at higher time resolution as seen in the bottom panel of Figure 4. The higher S/N data from the coherently dedispersed observations allow us to probe eclipses at time resolution of 26 s as compared to the 591–624 MHz incoherently dedispersed data which has time resolution of 2.3 minutes. These observations equipped with higher time resolution and enhanced sensitivity (due to wider bandwidth) reveal a maximum excess DM of 0.035(3) pc cm^{-3} and N_e of $10.8(8) \times 10^{16}$ cm^{-2}. We estimate the corresponding electron density in the eclipse region ($n_e \sim N_e/2a$) as 0.3×10^6 cm^{-3}, which is at least an order of magnitude higher than the electron density in the stellar wind (according to Johnstone et al. 2015 n_e due to stellar wind at a distance similar to separation between companion and inferior conjunction is $\sim 10^4$ cm^{-3}).

3.4. Continuum and Pulsed Flux

Aided by the capability of simultaneously recording visibilities along with the tied-array coherent beam from the GMRT interferometer, we estimated flux densities around eclipse boundaries using continuum imaging and compared that with the pulsed flux densities. Unlike pulsed flux densities the flux densities obtained from continuum imaging are expected to be unaffected by the temporal smearing caused by excess dispersion and/or scattering. This comparative study of continuum and pulsed flux densities can be used for understanding the eclipse mechanism, which was done by Roy et al. (2015) for PSR J1227−4853, while probing the egress boundary. Apart from PSR J1227−4853, imaging studies for eclipsing binaries were done by Polzin et al. (2020) for PSRs B1957+20 and J1816+4510, by Polzin et al. (2018) for PSR J1810+1744 and by Broderick et al. (2016) for PSR J2215+5135.

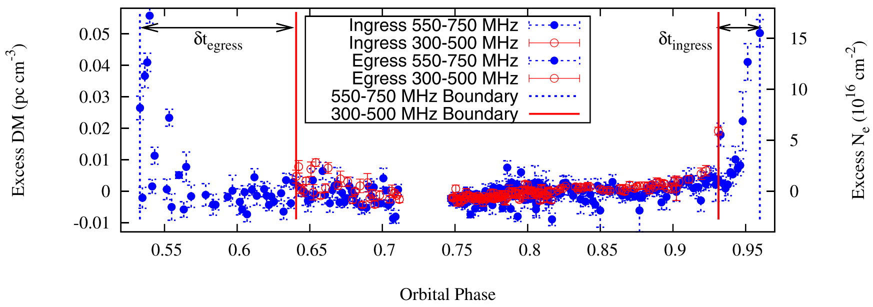

Figure 3. Variation of excess DM and Ne at eclipse egress and ingress boundaries measured simultaneously at 300–500 MHz (hollow red circles) and 550–750 MHz (filled blue circles). One epoch covers egress (2019 May 24) from orbital phase 0.53–0.82 and another covers ingress (2019 May 14) from orbital phase 0.80–0.96. A break seen in egress observation at orbital phase ∼0.72 is due to rephasing of the array.

Table 1
Parameters for Eclipsing Binary Millisecond Pulsar Systems Listed in Column 1 Indicating Its Type, Redback (RB), or Black Widow (BW)

Pulsar Name	Excess DM (pc cm^{-3})	$\dot{E}/a^2$ [a] (10^{35}) (erg/s/$R_\odot^2$)	Eclipse Duration[b]	n	Reference[c]
J1023+0038 (RB)	0.15(700)	0.33	40(685)	−0.41	1
J1048+2339 (RB)	0.008(327)	0.03	57(327)	…	10
J1227−4853(RB)	0.079(607)	0.29	64(607)	−0.44	2
J1227−4853[d] (RB)	0.035(607)	…	6(607)	…	2
J1544+4937 (BW)	0.027(607)	0.11	13(322)	…	3
J1723−2837 (RB)	…	0.04	26(1520)	…	4
B1744−24A (RB)	0.6(1499.2)	…	∼50[e](820)	…	5
J1810+1744 (BW)	0.015(325)	0.18	13(149)	−0.41	6
J1816+4510 (RB)	0.01(149)	0.08	24(121)	−0.49[f]	8
B1957+20 (BW)	0.01(149)	0.22	18(121)	−0.18	8
J2051−0827 (BW)	0.13(705-4023)	0.06	28(149)	−0.41	7, 8
J2215+5135 (RB)	…	0.28	66(149)	−0.21[f]	8, 9

Notes. Column 2 presents the excess dispersion. Column 3 presents $\dot{E}/a^2$, where $\dot{E}$ is spin-down energy of the pulsar and a is distance to the companion. Column 4 presents eclipse duration with corresponding frequency in parentheses. Column 5 denotes the index of power-law dependence (n) of full eclipse duration with frequency.
[a] Using https://apatruno.wordpress.com/about/millisecond-pulsar-catalogue/.
[b] The eclipse duration (in percent of orbit) includes nondetection and associated ingress and egress transition.
[c] List of references: (1) Archibald et al. (2009); (2) current work; (3) Bhattacharyya et al. (2013); (4) Crawford et al. (2013); (5) Bilous et al. (2019); (6) Polzin et al. (2018); (7) Polzin et al. (2019); (8) Polzin et al. (2020); (9) Broderick et al. (2016); (10) Deneva et al. (2016).
[d] Parameters for excess dispersion observed around the inferior conjunction.
[e] For the majority of observed eclipses. However, observed eclipse durations are variable and sometimes completely enshrouding the pulsar (Bilous et al. 2019).
[f] The value of the estimated power-law index using all available frequency measurements as given in the recent literature.

For PSR J1227−4853 we analyzed the imaging data (details in Section 2) to produce a lightcurve for the pulsar signal during eclipse ingress and during the instances of excess dispersion around inferior conjunction. The top panel of Figure 5 shows the continuum (marked in blue) and pulsed (marked in green) flux densities as a function of orbital phase for an eclipse ingress. A curve showing the timing residuals (marked in red) reaching up to $404 \pm 46\,\mu$s is also added in this plot. The continuum and pulsed flux densities show correlated changes as the pulsar is transitioning into eclipse at $\phi_B \sim 0.03$, where the timing residuals are rapidly increasing. We have carried out a similar lightcurve analysis for the 2018 December 2 event of excess dispersion around $\phi_B = 0.8$. As seen in the bottom panel of Figure 5, the TOAs (red curve) are delayed by about $307 \pm 11\,\mu$s at $\phi_B = 0.8$. The continuum flux density (blue curve) and pulsed flux density (green curve) fade in anticorrelation with the arrival times. The region with the excess dispersion delay is highlighted in the bottom panel of Figure 5. The two peaks of timing residual at $\phi_B = 0.783$ and 0.805 are exactly coinciding with two dips of the continuum and pulsed flux densities. The observed continuum flux density at $\phi_B = 0.805$ is around 30% of the peak continuum flux density measured at orbital phase $\phi_B = 0.825$. Overall the pulsed flux density is consistent with the continuum flux density. For the orbital range of 0.79–0.8 the pulsed flux density is a little bit lower than the continuum flux density. This could be due to the presence of temporal broadening caused by increased DM as also seen in Polzin et al. (2020). We performed lightcurve measurements of nearby point sources within the field of view showing no significant variation of flux densities over the observing span. We observed scintles of a few MHz in size, as well as flux brightening of a few minutes in duration on both sides of the event of excess dispersion (orbital phase ∼0.805), which can explain the enhancement of flux densities (highlighted region in the bottom panel of Figure 5).

4. Discussion and Summary

We find that during ingress and egress the pulses are significantly delayed relative to the best-fit timing model. The largest timing residual deviation that we measure is 888(28) μs.

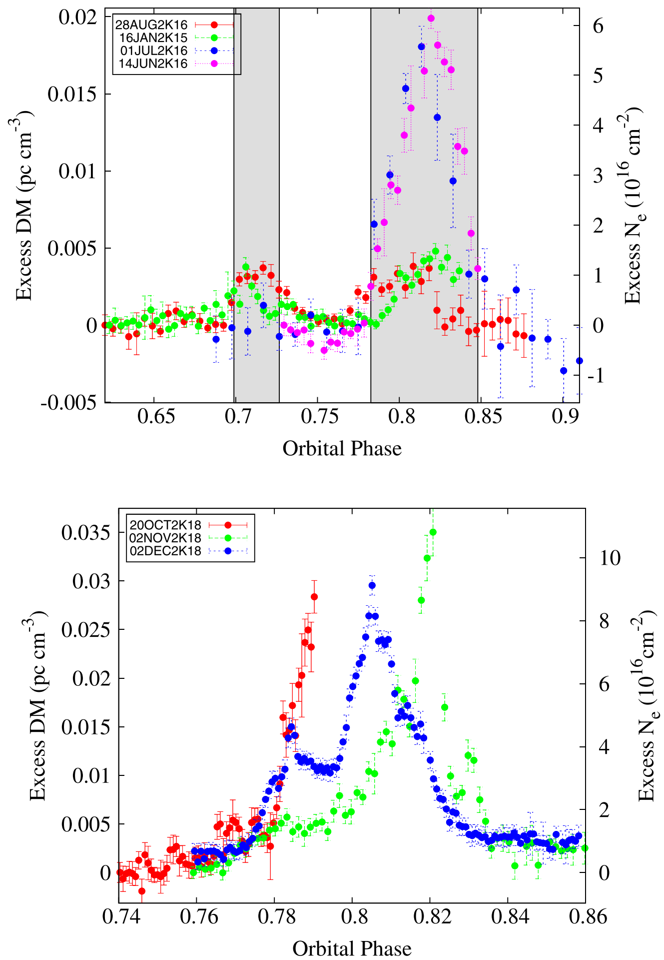

Figure 4. Top panel: variation of excess DM and N_e measured around orbital phase 0.7 and 0.8 at 591–624 MHz with time resolution of 2.3 minutes. Bottom panel: variation of excess DM and N_e measured around orbital phase 0.8 at 550–750 MHz with coherently dedispersed observations with time resolution of 26 s. More sensitive data with higher time resolution brings out the pattern of variation of excess N_e with orbital phase.

We estimate excess DM and N_e as $0.079(3)\,\mathrm{pc\,cm^{-3}}$ and $24.4(8)\times10^{16}\,\mathrm{cm^{-2}}$ respectively. The eclipse duration including the ingress, egress transition for PSR J1227−4853 is about 265 ± 3 minutes (64% of its orbit), indicating that for a larger fraction of its orbit the pulsar is enshrouded by the intra-binary materials. From Table 1 we note that the observed values of excess DM, N_e, eclipse duration, and $\dot{E}/a^2$ for PSR J1227−4853 are similar to PSR J1023+0038, which is the other LMXB−MSP transitioning system. An asymmetry is seen between egress and ingress duration, with egress being longer by 12.4 ± 3 minutes. This asymmetry can be caused by a tail of eclipsing material swept back due to orbital motion of the companion, which is also observed for other eclipsing binaries (e.g., Polzin et al. 2020). Such asymmetries can be generated by the interaction of outflowing gas from the companion with pulsar radiation, which can create increased density in the trailing part of the outflow as shown using the hydrodynamical simulation by Tavani & Brookshaw (1991), suggesting this as the explanation for the observed eclipses of PSR B1957+20 (Fruchter et al. 1990). From the dual frequency observations on two epochs one covering egress boundary and another covering ingress boundary, we observed that 300–500 MHz eclipse duration is longer than 550–750 MHz. A longer eclipse

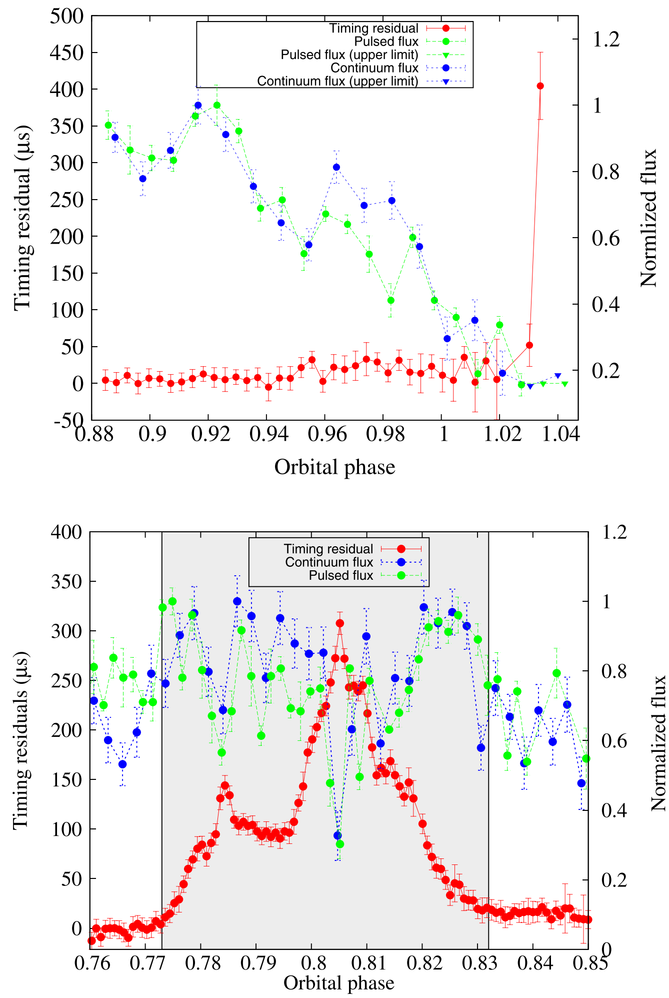

Figure 5. Top panel: variation of timing residuals (added to mark the start of the eclipse) and flux densities (both pulsed and continuum) with orbital phase during ingress at 550–750 MHz observed on 2019 January 1. Bottom panel: variation of timing residuals and continuum flux densities with orbital phase around inferior conjunction at 550–750 MHz observed on 2018 December 2. The highlighted region indicates the anticorrelated variation of continuum flux with timing residuals.

duration at lower frequencies is also observed for other eclipsing binaries (Stappers et al. 2001; Broderick et al. 2016; Polzin et al. 2018, 2020). In addition we observe that for PSR J1227−4853 the ingress boundary starts earlier (∼11.9 minutes) and egress ends later (∼44.6 minutes) at lower frequency (300–500 MHz) than at higher frequency (550–750 MHz), i.e., $\delta t_{\mathrm{egress}} > \delta t_{\mathrm{ingress}}$ by 32.7 ± 0.7 minutes.

We estimate the power-law index for the frequency dependent eclipse duration as $n=-0.44$. From Table 1, we generally find that redback pulsars have a relatively longer eclipse duration and excess DM at the eclipse boundaries compared to the black widow systems. Future study of a statistically significant sample of such eclipsing binaries over a wide frequency range is warranted for better understanding.

We observe a fading of the pulsar flux density around the inferior conjunction ($\phi_B\sim0.7$ & 0.8) that is also associated with an excess timing delay on several occasions (∼25% of all observations). To our knowledge such systematic change of flux density around a fixed orbital phase (i.e., inferior conjunction in this case) is not reported for any other eclipsing binary. Occasional clustering of fragmented blobs of plasma around the inferior conjunction could possibly lead to such a decrease in flux. The maximum value of excess DM and N_e observed around inferior conjunction ($\phi_B = 0.82$) is a factor of two to four times lower than that observed at the eclipse boundary for PSR J1227−4853. In this context we note that for PSR J1544+4937 (having very similar excess DM and N_e as seen in PSR J1227−4853) frequency dependent eclipsing around superior conjunction is observed, where the pulsed signal exhibits a decrease in flux at higher frequency (∼607 MHz) and is completely eclipsed at lower frequency (∼322 MHz) as reported by Bhattacharyya et al. (2013). Future investigations of PSR J1227−4853 at lower frequencies may reveal frequency dependent eclipsing around the inferior conjunction. Short eclipses are generally seen around the eclipse region centered on the superior conjunction in other eclipsing binaries, e.g., for PSR J1544+4937 by Bhattacharyya et al. (2013). However, for PSR J1227−4853 we observe the phenomenon of excess dispersion with flux fading preferentially centered around inferior conjunction. According to de Martino et al. (2015), the X-ray emission originates in an intrabinary shock produced by the interaction of the outflow from the companion and the pulsar wind. We also note that de Martino et al. (2015) observed a dip in the count rate centered at $\phi_B = 0.75$, while monitoring the X-ray orbital modulation of the pulsar. Radio observations reported in this paper have at least an order of magnitude better orbital phase resolution than the X-ray observations, which possibly allowed us to resolve the single dip seen in X-ray in two symmetric dips observed in radio around inferior conjunction. Tavani & Brookshaw (1991) explained the observed eclipse properties for PSRs B1957+20 and B1744−24A using hydrodynamical simulations of the companion's wind outflow. They showed that the eclipses are created due to the shocks generated by interaction between the pulsar radiation and the outflowing gas from the companion star. They explained drastic eclipse changes observed for PSR B1744−24A by Lyne et al. (1990), while inferring that the eclipse shape is dependent on the thermal and kinetic state of the outflowing gas, which could be time variable. By progressively decreasing the mass loss rate Tavani & Brookshaw (1993) arrived at a final mass configuration allowing the pulsar to be visible for a large fraction of the orbital phase. Whereas for progressively increasing or for a constant but relatively large value of the mass loss rate, the pulsar could get completely enshrouded. According to Itai Linial (2017) mass transfer through L2 Lagrangian point could happen for a system having rapid orbital evolution. In the case of PSR J1227−4852 mass transfer during the accretion phase through L2 could be responsible for material floating around the inferior conjunction causing excess dispersion. The observed occasional flux fading around the inferior conjunction for J1227−4853 could also be caused by systematic changes in final mass configurations achieved via variations in the mass loss rate or other parameters such as temperature or Mach number. Frequent multifrequency observations are planned to probe this in more detail.

From simultaneous timing and imaging analyses we find that pulsed and continuum flux densities of PSR J1227−4853 follow a similar trend at eclipse ingress. Roy et al. (2015) reported a similar finding at eclipse egress for the same pulsar. In earlier studies the decrease of continuum flux densities at eclipse boundaries were reported by Polzin et al. (2018) for PSR J1810+1744 and by Broderick et al. (2016) for PSR J2215+5135. We also measure the variations of continuum flux densities around the inferior conjunction (presented in Section 3.3) and find that the minima in continuum flux density coincides with the maxima in excess dispersion.

Now we investigate possible eclipse mechanisms following Thompson et al. (1994). In order to study the pulse smearing due to dispersion as a cause of the eclipse, DM ∼ 1.3 pc cm^{-3} is required to disperse pulsed emission completely. However, the measured largest excess DM at the eclipse boundary is 0.079(3) pc cm^{-3}, which is a factor of ∼16 less, and hence rule out the dispersion as the cause of eclipse. The scattering due to excess N_e can broaden the pulse and change the pulse profile. However, we have not seen any signature of profile evolution at eclipsing boundaries. Thus scattering as a cause is ruled out. Moreover, temporal smearing due to the dispersion or scattering is not expected to change the continuum flux density. For refraction to be the cause of the eclipse the expected group delay at the ingress or egress would be ∼10–100 ms as reported by Thompson et al. (1994). We measure maximum time delay around eclipse boundary ∼888 μs, for PSR J1227−4853, which is at least an order of magnitude smaller than the group delay required for refraction of the radio beam causing eclipse. This implies refraction cannot be the cause of eclipse. For an eclipsing binary system with temperature T and clumping factor of the eclipsing medium $f_{\rm cl}$ ($f_{\rm cl} = \langle n_e^2\rangle / \langle n_e\rangle^2$), the optical depth due to free–free absorption is given by Equation (1) (Thompson et al. 1994), where N_e is electron column density and L is absorption length.

$$\tau_{\rm ff} \simeq 3.1 * 10^{-8} \frac{f_{\rm cl}}{T_7^{3/2}} N_{e,17}^2 L_{11}^{-1}. \quad (1)$$

Using Equation (1) we derive, $T \leqslant 10^2 \times f_{\rm cl}^{2/3}$ K, as the relation between the temperature T and clumping factor of the eclipsing medium. This indicates that for free–free absorption to be the cause of eclipse (i.e., $\tau_{\rm ff} > 1$) in PSR J1227−4853 with $N_e = 24.4 \times 10^{16}$ cm^{-2} at eclipse boundary and absorption length about twice the size of the eclipse zone, we need either a very high clumping factor or a very low temperature. Assuming a temperature range from an unheated star to an irradiated star (i.e., 5500–500,000 K) according to de Martino et al. (2014), we expect the range of the clumping factor to be 400 to 3.5×10^5, which is not physically possible (Muijres et al. 2012), ruling out free–free absorption as the cause of eclipse. Considering PSR J1227−4853 has an average flux density at 650 MHz (S_ν^0) ∼1.2 mJy, spectral index (α) $\geqslant -1.8$ and distance ($d_{\rm kpc}$) ∼1.4 kpc, and demagnification (M) $\sim (R_c/2r)^2$, where R_c is the radius of curvature of the plasma cloud and r is the distance from the center of the curvature, the induced Compton optical depth can be calculated with Equation (2) (Thompson et al. 1994).

$$\tau_{\rm ind} \simeq 4 * 10^{-5} \frac{N_{e,17}^2 S_\nu^0}{\nu_9^2} |\alpha + 1| \left(\frac{d_{\rm kpc}}{a_{11}}\right)^2 M. \quad (2)$$

We calculate the upper limit of induced Compton depth $\tau_{\rm ind} \leqslant 7.6 \times 10^{-5}$, which rules out induced Compton scattering to be the cause of the eclipse. The decrease of continuum flux density at eclipse boundary as well as flux fading around inferior conjunction indicates absorption of pulsar flux by line-of-sight material could be a plausible cause of eclipse. In order to check if cyclotron–synchrotron absorption of pulsar emission by nonrelativistic or relativistic electrons is the cause of the eclipse we estimate the magnetic field of the eclipsing plasma with Equation (3) (Thompson et al. 1994), where $m = \nu/\nu_B$, $\omega_B = 2\pi\nu_B = eB/m_e c$.

$$B = 350m^{-1}\nu_9 \text{ G}. \quad (3)$$

We calculate the magnetic field in the vicinity of the companion to be 27 G, and the cyclotron fundamental frequency to be 77 MHz. Observed eclipses reported in this paper for PSR J1227−4853 are centered at 322 and 607 MHz, which are fourth and eighth harmonics of this cyclotron fundamental frequency. In this context, we note that eclipses for PSR J1544+4937 have been seen up to the twentieth harmonic of its fundamental cyclotron frequency (Bhattacharyya et al. 2013). For PSR J1227−4853 cyclotron absorption at fundamental cyclotron frequency and its lower harmonics can be the cause of eclipse. The observed larger frequency dependence of the eclipse egress compared to the ingress can also be explained by the the presence of more stellar material around the eclipse egress than ingress, which could result into enhanced frequency dependence of cyclotron absorption optical depth. Since cyclotron absorption optical depth decreases for higher harmonics, it will be useful to probe the eclipse phase for this pulsar at higher frequencies. We plan to estimate the companion's magnetic field near the eclipse boundaries via studying the variation of rotation measure values (Li et al. 2019; Polzin et al. 2019).

To summarize, in this paper we report a detailed multi-frequency study of the eclipse properties for PSR J1227−4853. In addition to regular eclipses around superior conjunction, the system also shows evidence of excess dispersion and flux fading around inferior conjunction. Simultaneous studies of pulsed and continuum flux densities indicate flux removal possibly due to the cyclotron absorption rather than temporal smearing as the cause of eclipse, both for regular eclipse as well as for flux fading at inferior conjunction.

We acknowledge support of the Department of Atomic Energy, Government of India, under project No. 12-R&D-TFR-5.02-0700. B.W.S. acknowledges funding from the European Research Council (ERC) under the European Union's Horizon 2020 research and innovation programme (grant agreement No. 694745). The GMRT is run by the National Centre for Radio Astrophysics of the Tata Institute of Fundamental Research, India. We acknowledge the support of GMRT telescope operators for observations. We acknowledge discussions with Devojyoti Kanasabanik.

ORCID iDs

Sanjay Kudale https://orcid.org/0000-0002-6631-1077
Jayanta Roy https://orcid.org/0000-0002-2892-8025
Bhaswati Bhattacharyya https://orcid.org/0000-0002-6287-6900
Ben Stappers https://orcid.org/0000-0001-9242-7041
Jayaram Chengalur https://orcid.org/0000-0002-0269-1154

References

Archibald, A. M., Stairs, I. H., Ransom, S. M., et al. 2009, Sci, 324, 1411
Bhattacharya, D. 1992, ASIC, 377, 257
Bhattacharyya, B., Roy, J., Ray, P. S., et al. 2013, ApJL, 773, 12
Bilous, A. V., Ransom, S. M., & Demorest, P. 2019, ApJ, 877, 125
Broderick, J. W., Fender, R. P., & Breton, R. P. 2016, MNRAS, 459, 2681
Chengalur, J. N. 2013, Technical Report NCRA/COM/001
Crawford, F., Lyne, A. G., Stairs, I. H., et al. 2013, ApJ, 776, 20
de Martino, D., Casares, J., Mason, E., et al. 2014, MNRAS, 444, 3004
de Martino, D., Papitto, A., Belloni, T., et al. 2015, MNRAS, 454, 2190
Deneva, J. S., Ray, P. S., Camilo, F., et al. 2016, ApJ, 823, 105
Eggleton, P. P. 1983, ApJ, 268, 368
Fruchter, A. S., Berman, G., Bower, G., et al. 1990, ApJ, 351, 642
Fruchter, A. S., Gunn, J. E., Djorgovski, S. G., et al. 1988, IAUC, 4617, 1
Gupta, T., Ajithkumar, B., & Kale, H.S. 2017, CSci, 113, 707
Itai Linial, R. S. 2017, MNRAS, 469, 2441
Johnstone, C. P., Güdel, M., Lüftinger, T., et al. 2015, A&A, 577, 27
Li, D., Lin, F., & Main, R. 2019, MNRAS, 484, 5723
Lyne, A. G., Manchester, R. N., D'Amico, N., et al. 1990, Natur, 347, 650
Main, R., Yang, I-S., Chan, V., et al. 2018, Natur, 557, 522
Mohan, N., & Rafferty, D. 2015, PyBDSF: Python Blob Detection and Source Finder, Astrophysics Source Code Library, ascl:1502.007
Muijres, L. E., Vlink, J. S., de Koter, A., et al. 2012, A&A, 526, A32
Nice, D. J., & Thorsett, S. E. 1992, ApJ, 397, 249
Polzin, E. J., Breton, R. P., Bhattacharyya, B., et al. 2020, MNRAS, 494, 2948
Polzin, E. J., Breton, R. P., & Clarke, A. O. 2018, MNRAS, 476, 1968
Polzin, E. J., Breton, R. P., Stappers, B. W., et al. 2019, MNRAS, 490, 889
Ransom, S. M., Eikenberry, S. S., & Middleditch, J. 2002, AJ, 124, 1788
Roy, J., Gupta, Y., Ue-Li, P., et al. 2010, ExA, 28, 25
Roy, J., Ray, P. S., Bhattacharyya, B., Stappers, B., et al. 2015, ApJL, 800, 12
Ryba, M. F., & Taylor, J. H. 1991, ApJ, 371, 739
Stappers, B. W., Bailes, M., Lyne, A. G., et al. 2001, MNRAS, 321, 576
Stappers, B. W., Bails, M., Lyne, A. G., et al. 1996, ApJ, 465, 119
Tavani, M., & Brookshaw, L. 1991, ApJ, 381, 21
Tavani, M., & Brookshaw, L. 1993, A&A, 267, 1
Thompson, C., Blandford, R. D., Evans, C. R., et al. 1994, ApJ, 422, 304